Investigation of the transition from streamer to uniform ‘overvoltage’ mode of atmospheric air nanosecond-pulsed dielectric barrier discharge

Investigation of the transition from streamer to uniform "overvoltage" mode of atmospheric air nanosecond-pulsed dielectric barrier discharge

Chong Liu, Alexander Fridman, Danil Dobrynin

C&J Nyheim Plasma Institute, Drexel University, Camden NJ, USA

Abstract

A nanosecond-pulsed dielectric barrier discharge ignited in atmospheric air was studied by optical emission spectroscopy to investigate the time- and space-resolved development of the reduced electric field. The discharge operated in two distinct modes that correlate with the values of the applied electric field: non-uniform streamer regime and uniform breakdown regime. It is shown that the reduced electric field in the non-uniform mode corresponds to the propagation of cathode-directed streamers, while in uniform discharge both molecular nitrogen emission and the reduced electric field are uniformly distributed along the gap during the initial discharge development stage with corresponding lower reduced electric field values.

Introduction

Uniformity of high-pressure discharges, especially those ignited in air, has been a topic of interest for long time. Conventionally, as the applied electric field (voltage) increases, the breakdown mechanism changes from uniform Townsend discharge to non-uniform streamer discharge. Previously, we have put forth a hypothesis that with application of significant overvoltages, i.e., fast rising pulsed electric fields that allow production of electron density suitable for avalanche-streamer transition significantly before the discharge gap is bridged, may result in development of spatially uniform plasma [1-3]. It must be noted, that "significant overvoltage mode" we define the conditions when the transition from the streamer regime occurs, and in our experimental conditions (room air, low energy pulses of few mJ) the value is above ~130 kV/cm [2, 3]. This study is devoted to further understand the time and space evolution of the reduced electric fields in the atmospheric air conventional DBD and DBD ignited under overvoltage conditions.

Atmospheric air dielectric barrier discharge (DBD) are one of the traditional ways to generate non-thermal plasma for various applications [4, 5]. Conventional air DBD, - for example, those that are driven by sinusoidal high voltage power supplies, - operates in a conventional breakdown regime via development of cathode-directed streamers which later, due to charge deposition and other possible memory effects, result in formation of filaments [4-6]. Filamentation of the DBD results in excessive gas heating in microdischarge channels and non-uniform discharge energy distributions, thus limiting potential applications. In order to avoid these adverse effects, DBD plasma can be uniformly ignited by using higher repetition rate high voltage pulses (this method allows higher preionization levels, and ignition of "streamerless" DBD), choosing appropriate gas mixtures (slowing down ionization rate), or decreasing gas pressures, effectively avoiding avalanche-streamer transition [6 – 13]. In our previous

studies [2, 3], we have shown that application of fast over-voltages may result in generation of a uniform DBD plasma when avalanche-streamer transition happens significantly earlier, before the initial avalanche reaches the anode. In [2, 3] we have shown that the discharge uniformity may be achieved in the case strong overvoltage in the discharge gap (provided by fast rise times).

In this study we attempt to study the development of the atmospheric air nanosecond-pulsed dielectric barrier discharge by measuring the development of the reduced electric field (REF) in the cases of uniform and non-uniform DBD modes. Although other, for example, laser-based methods (four-wave mixing) for measurement of electric field offer better sensitivity and time resolution can be applied for determination of electric fields prior any photon generation in the discharge gap [14-19], here we utilize the approach of estimation of the reduced electric field strength values from the ratio of the emission intensities of the vibrational bands of nitrogen using ICCD camera with sub-nanosecond time resolution. This method allows us to estimate the reduced electric field values in 2D geometry (without consideration of the issues associated with actual 3D emission and other limitations of this method – see discussion, for example, in [20, 21]).

Experimental setup and methods

The pulse generating, monitoring and triggering was performed as described in [2] and [3] (Figure 1). Briefly, the pulsed high voltage power supply (FID Tech Company) generated pulses were delivered to the electrodes via $100 ft$ of $RG\ 393/U$ 50 Ohm high voltage coaxial cable. Pulse shape monitoring, and camera triggering was done using a return current shunt was mounted $22\ ft$ from output of the power supply. The dielectric barrier discharge was ignited in a sphere-to-plate geometry with a plane high-voltage electrode diameter of 2.4 cm covered with 1 mm thick quartz and the grounded bronze hemisphere with diameter of 5 cm. Inter-electrode gap was changed between 1 and 3 mm, and the discharge was ignited in room air conditions. FID pulsed power supply was used to generate high voltage pulses with maximum amplitude at the high voltage electrode of 23.3 kV, pulse rise time of 1.6-2.2 ns (10 - 90% peak amplitude) and 12.3 ns duration (63% amplitude). Pulse frequency was set at 10 Hz to avoid the effects of charge accumulation and associated “memory” effects. Applied electric field values were calculated according to the expressions in [2] assuming the peak value of the voltage pulse.

The emission from the discharge was focused onto the entrance slit of the first stage of the Princeton Instruments TriVista 555 spectrometer using 25-mm quartz lens system, Newport (entrance slit was set to 10 μm and 1800 g/mm grating was used, spectral resolution was 0.1 nm). Emission spectra were recorded using 4Picos ICCD camera (Stanford Computer Optics). System spectral response was calibrated using 63978 NIST Traceable Quartz Tungsten Halogen Calibration Source, Newport. Triggering and time monitoring was done using Tektronix AFG 3252 Arbitrary function generator and Tektronix DPO4104B Oscilloscope.

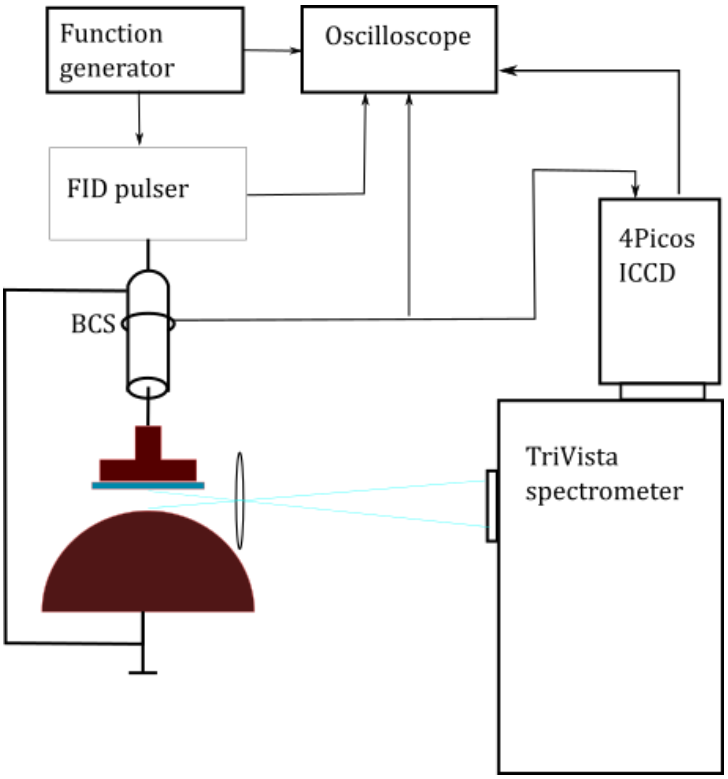

Figure 1. Experimental setup schematic.

To determine the development of the electric filed strength in the discharge (E/n), we recorded emission spectra of the second positive (SPS) vibrational transitions of nitrogen and the first negative (FNS) of N_2^+ with central wavelengths at 337.1 nm and 391.5 nm respectively. Each spectrum was recorded by ICCD camera with 100 accumulations; 0.2 ns exposure time (with 0.2 ns delay time step) for the initial stage of the discharge (first ignition) and 0.5 ns exposure time (with 0.5 ns delay time step) was used for samples during the dark period and the second stage (reignition on the trailing edge of the high voltage pulse) of the discharge. Sample emission spectra for 391.5 nm and 337.1 nm are shown in Figure 2. In all the plots. Recorded light outside of the discharge gap is due to reflections and curved surface of the ground electrode.

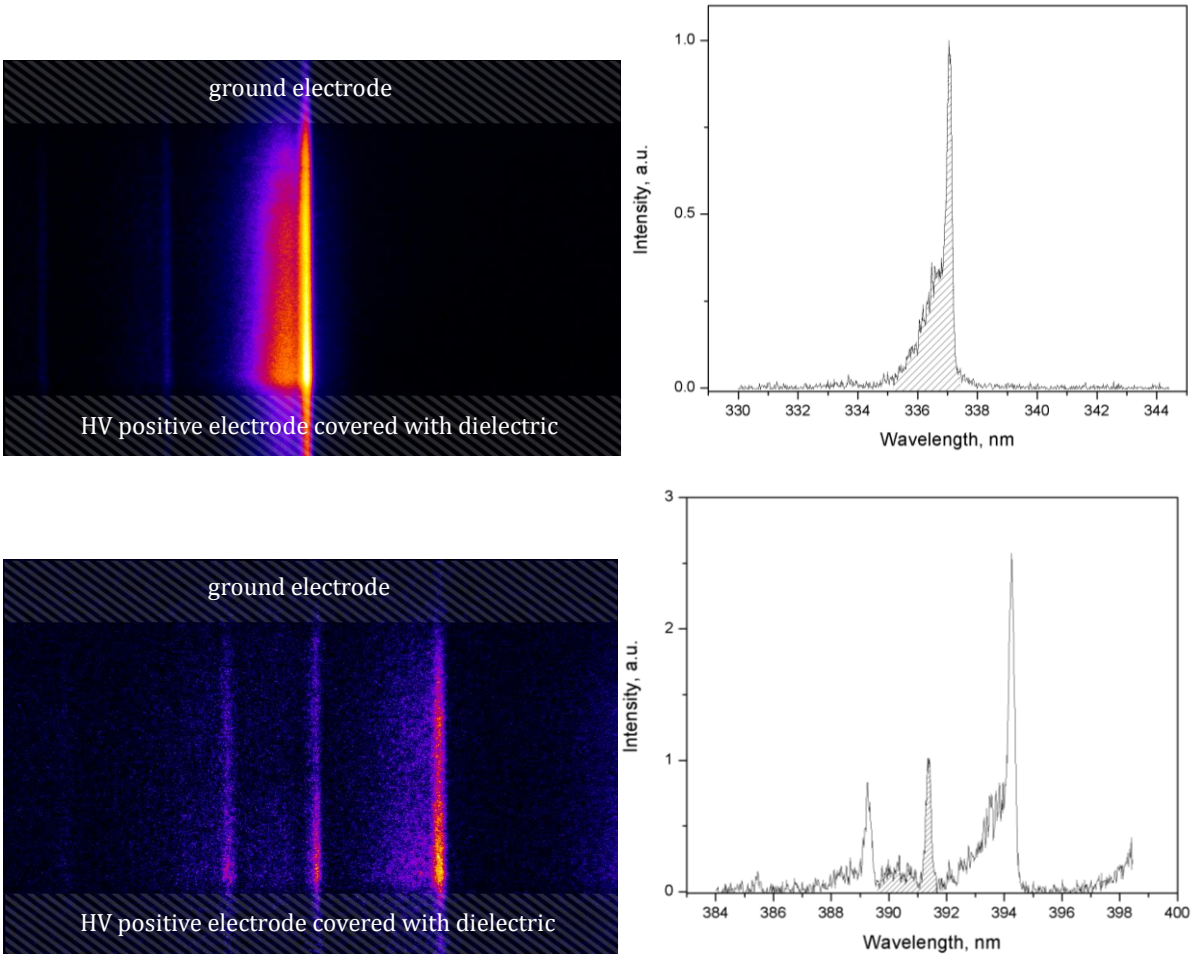

Figure 2. Typical image of the recorded spectra of the discharge for SPS (top) and FNS (bottom). Areas of integration for electric field measurements are shaded on graphs. Here: electrode gap 2 mm, delay time 2.9 ns; SPS spectrum graph is shown for row of pixels at around 0.2 mm from the ground electrode and FNS – around 0.5 mm from the high voltage electrode.

For the dynamic processes, time-dependent equation for the SPS and FNS intensity changes must be used [22-25]. Following the kinetic analysis presented in [23], here we have used the dynamic ratio in the following form:

$$\frac{\frac{dI(t)_{391}}{dt}+\frac{I(t)_{391}}{\tau_{391}}}{\frac{dI(t)_{337}}{dt}+\frac{I(t)_{337}}{\tau_{337}}}\cdot\frac{\tau_{391}}{\tau_{337}}=R_{391/337} \quad (1)$$

In this equation τ_{391} and τ_{337} are effective life time of two species and dt is chosen as the same as the sampling rate for intensity measurements. Here, following [15], we have used effective lifetimes of Dilesse et al [26]: $\tau_{391}=0.045\ ns$ and $\tau_{337}=0.64\ ns$. Before time and space-resolved intensities were fed into equation (1), every row of data was smoothed by moving average value with a window of 3 data points. In the case of intensity recording of the entire discharge (20 ns exposure time), the dynamic term $\frac{dI(t)}{dt}$ can

be ignored, and then equation (1) becomes just a ratio of two intensities. This ratio was calibrated by Paris et al [27]:

$$R_{391/337} = 46 \cdot 0.065 \cdot \exp[-89(E/n)^{-0.5} - 402(E/n)^{-1.5}]. \quad (2)$$

Following [15], we have used the relation (2) with a factor of 0.5 on the right-hand side. In order to check that this expression is valid for our experimental conditions, we have recorded time-integrated spectra of the discharge for uniform (1 mm gap) and non-uniform (3 mm gap) modes using triple stage of the TriVista system. Measured spectra were compared to Specair [28] simulations (Figure 3) and maximum temperature of the discharge was 330±20 K for 1 mm gap and 460±20 K for 3 mm gap. In this temperature regimes, the deviation from the experimental calibration curve should not result in significant deviations [27].

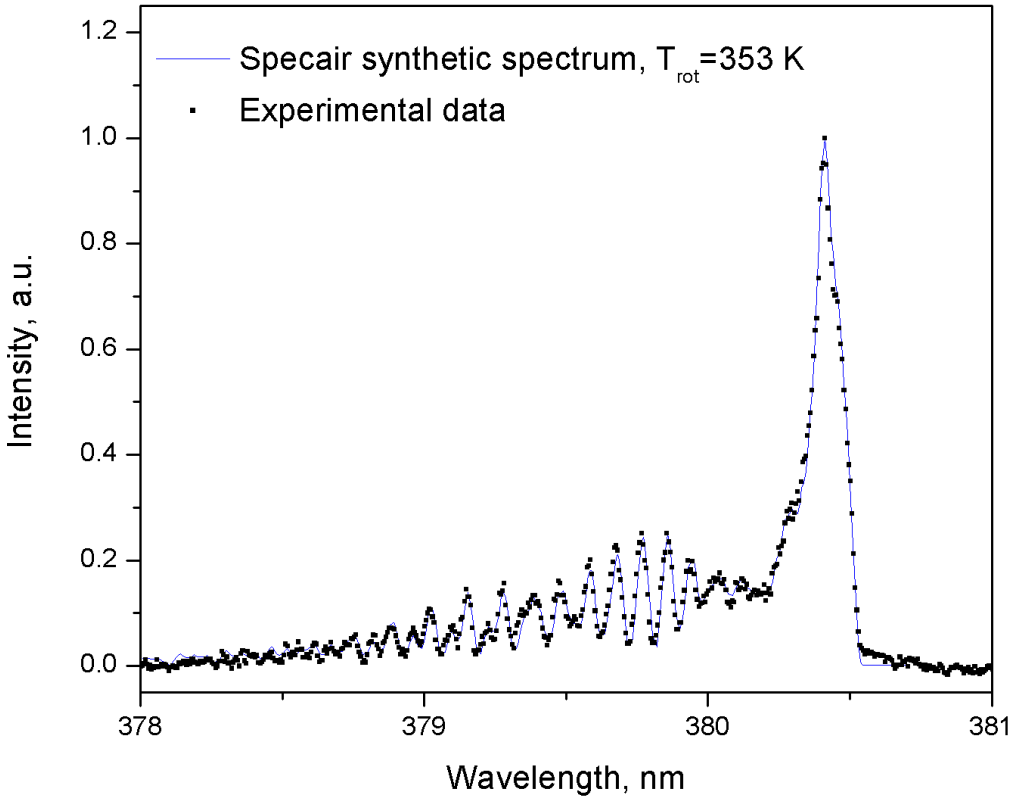

Figure 3. Specair [28] synthetic and experimentally measured spectrum for 1 mm discharge gap.

Results and discussion

Space-resolved dynamics of the wavelength integrated intensities of the SPS and FNS emissions are shown in Figures 4 and 5. Each value in data columns (time points) is the result of integration over the corresponding wavelength range shown in Figure 2, and its the vertical position corresponds to the light originating from the corresponding position in the discharge gap (i.e., each measured image on the left side in Figure 2 results in a single column shown in Figures 4 and 5). In these figures the emission was recorded with 200 ps exposure time and 200 ps delay step for the first 5 ns (discharge ignition on the rising edge of the high voltage pulse), and 500 ps exposure time and 0.5 ps delay step for the rest of the high voltage pulse duration. Each measurement is the result of 100 accumulations (to decrease signal-to-noise ratio). The emission presented in these figures corresponds to the discharge ignition on the rising and trailing edges of the high voltage pulse. The light emission that is recorded outside the discharge gap is due to the curvature of the second (grounded) electrode located in the upper part of the image, as well as some reflections from the quartz dielectric covering the high voltage electrode (bottom part of each image). It is interesting to note that in the case of shorter discharge gap distances (1 and 1.5 mm that correspond to applied electric fields around 184 and 132 kV/cm respectively) emission of the both SPS and FNS appear more uniform across the gap in the first and second discharge reignitions. In contrast, in longer interelectrode distances (2 and 3 mm, 103 and 71 kV/cm respective applied electric field) one can clearly see the development of cathode-directed streamers traveling towards the grounded electrode with the velocities of about 0.5-1×10^6 m/s. For the reignition stage on the trailing edge, similar effects are observed.

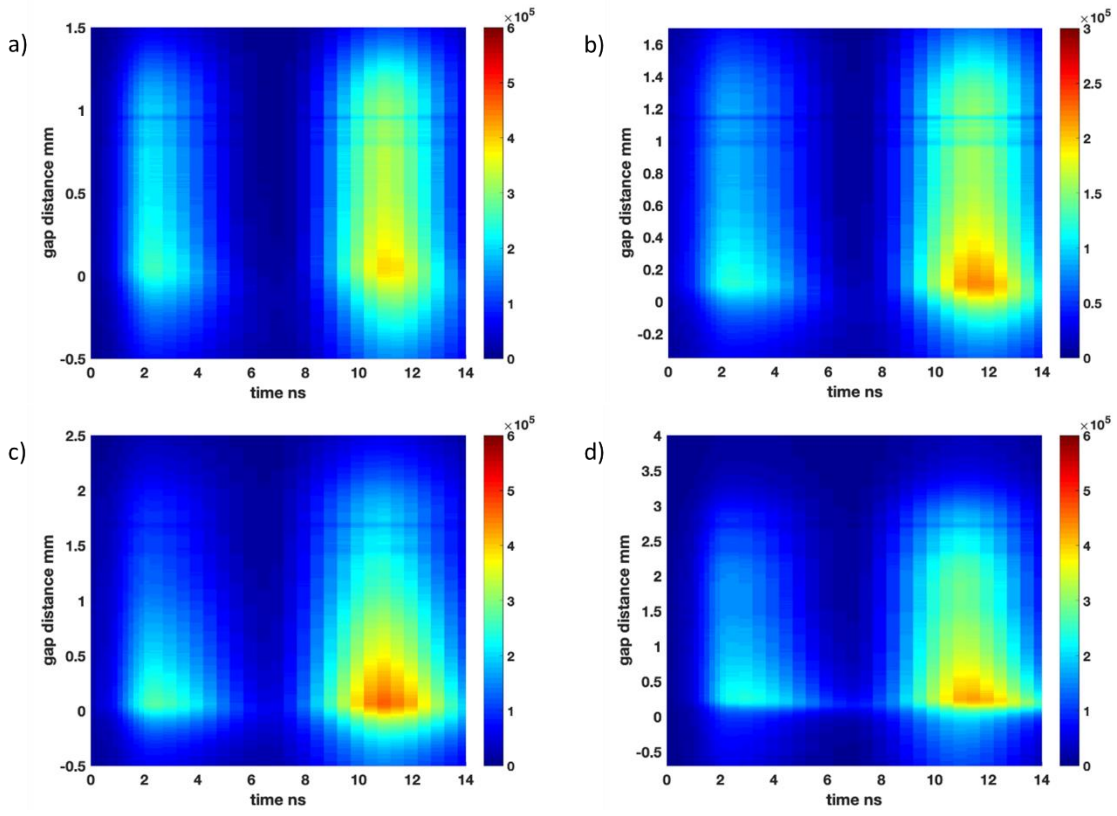

Figure 4. SPS at 337.1 nm development (false color) in nanosecond air DBD for different discharge gaps: a – 1 mm, b - 1.5 mm, c – 2 mm and d - 3 mm.

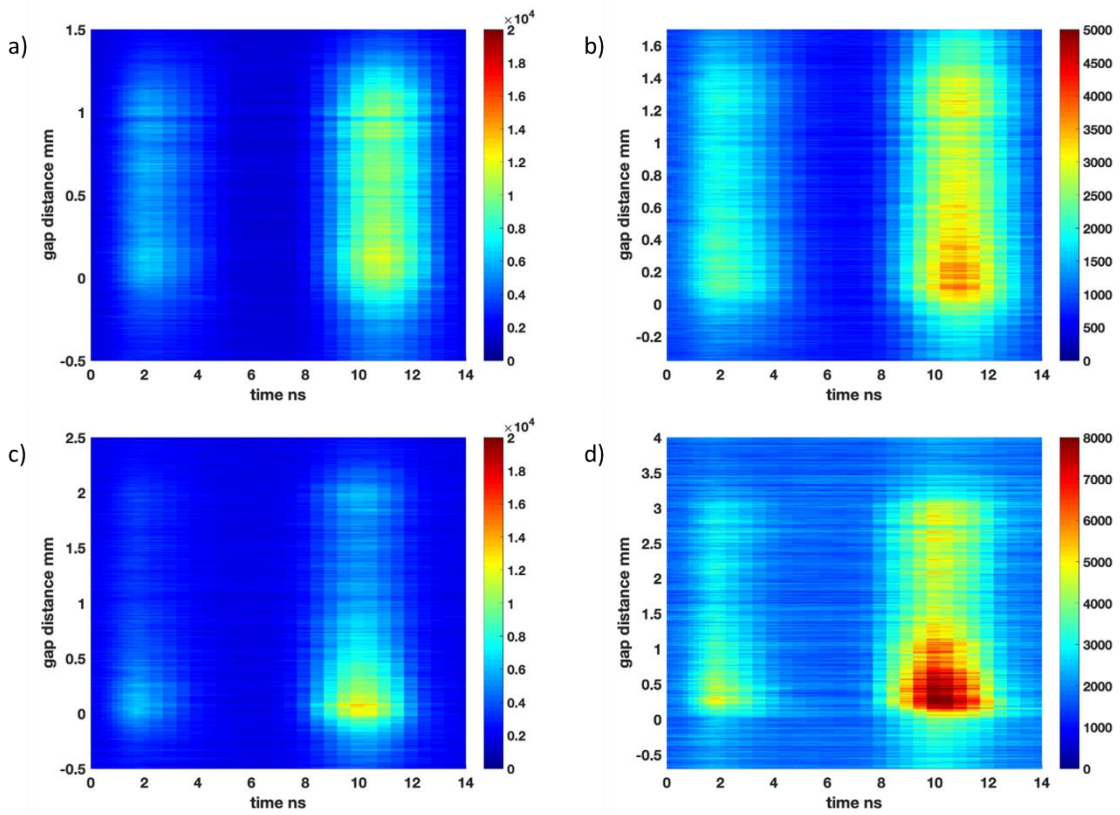

Figure 5. FNS and 391.5 nm development (false color) in nanosecond air DBD for different discharge gaps: a – 1 mm, b - 1.5 mm, c – 2 mm and d - 3 mm.

Figure 6 shows dynamics of integral (across the gap) intensities of SPS and FNS – the mutual time delay (shift) is clearly visible. Due to limitations of the time resolution of our system we estimate this delay to be on the order of 200 ps. More detailed measurements and analysis of this phenomenon can be found in [25].

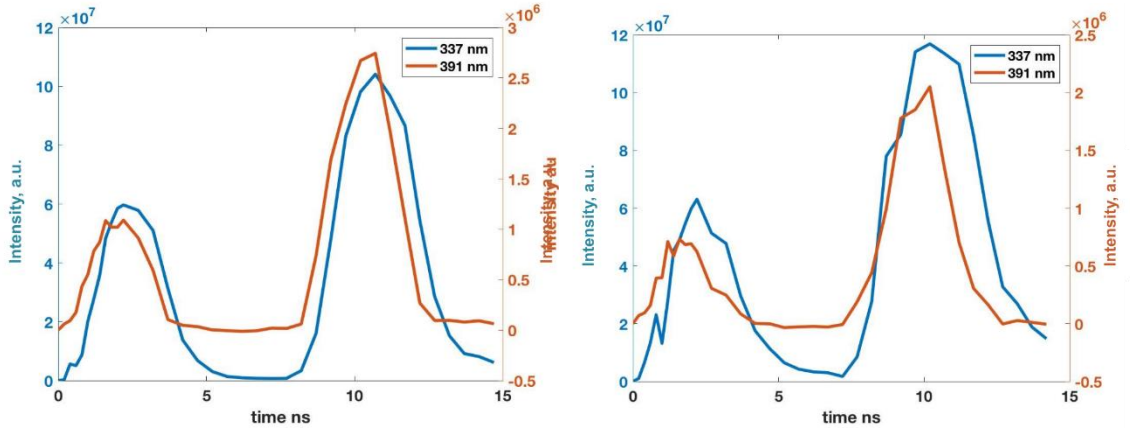

Figure 6. Time evolution of SMS and FNS emission for 1 mm (left) and 2 mm (right) discharge gaps. Mutual time delay of ~200-400 ps is clearly visible.

The development of the reduced electric field for different discharge gaps (and corresponding applied electric fields) is shown in Figure 7. The electric field values in the regions with weak FNS emission intensity (which results in abnormally high electric field values) were disregarded. Comparing the cases of 1 and 1.5 mm gap distances to 2 and 3 mm, it is clear that the peak values in the initial stage (around 0 – 1 ns) of the discharge are lower for the uniform discharge – around 800 and 1200 Td respectively. The same is observed for the reignition stage of the discharge. Similar values of the positive streamer head reduced electric field were reported previously [29-32]. Distribution of the reduced electric field along the gap is also non-uniform for the lower peak applied electric fields and represents development and propagation of cathode-directed streamers towards the ground electrode. It should also be noted that lower peak applied electric field means slower effective applied electric field rise time: for example, in the case of 1 mm discharge gap applied electric field rise time is ~88 kV/cm/ns, while for 3 mm - ~38 kV/cm/ns. Figure 8 shows zoomed in initial period of the discharge development. It is clear that at lower applied electric field values, the discharge develops via a conventional cathode-directed streamer mechanism, while at higher overvoltage values, an almost uniform discharge fills the gap. Long exposure (20 ns) spectra were also taken to estimate the average reduced electric field distribution along the gap using expression (2). From Figure 9, the average electric field along the gap showed two different distribution, which is coherent with two different operating regimes of atmospheric air DBD. We hypothesize, that initial avalanches in the latter case transition to streamer mode significantly earlier – before they reach the anode. These generally lower reduced electric values (Figure 9) indicate fast expansion of the plasma channels and their overlap, resulting in effectively absence of individual streamers and ignition of a uniform plasma.

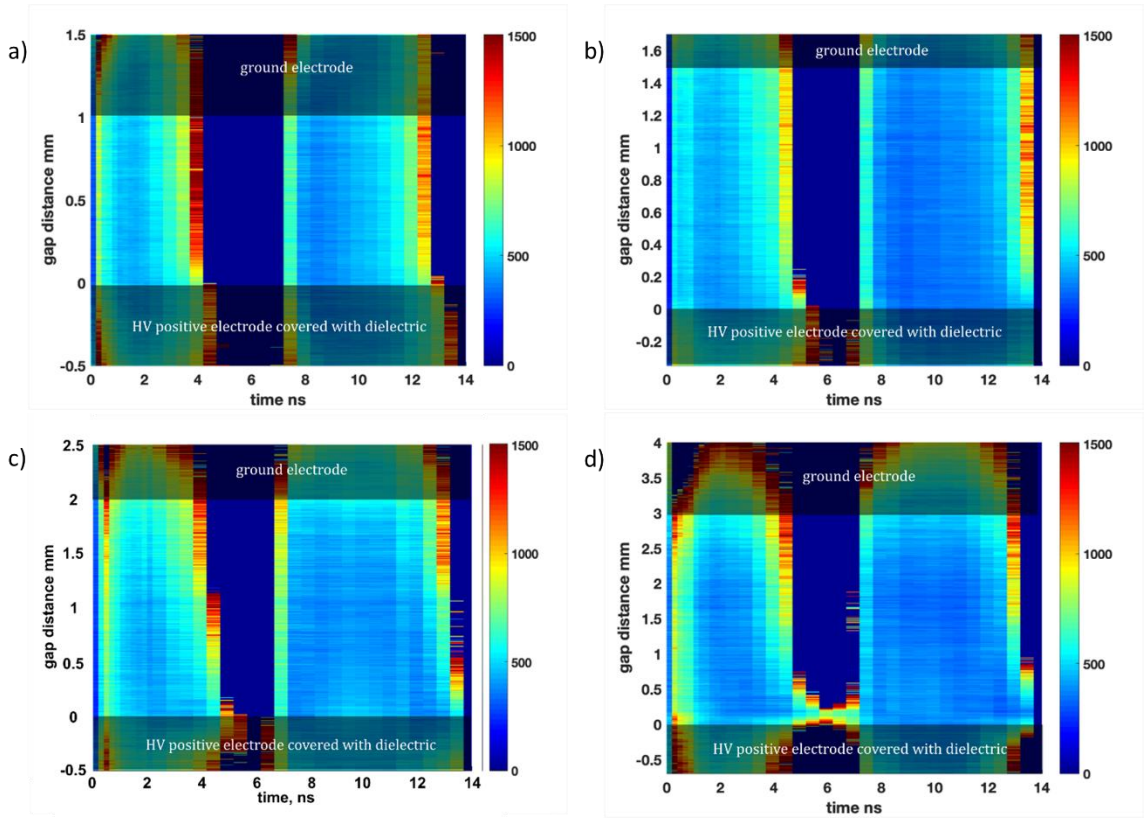

Figure 7. Reduced electric field evolution in the air DBD for different discharge gaps (maximum applied electric field): a - 1 mm (184 kV/cm), b - 1.5 mm (132 kV/cm), c - 2 mm (103 kV/cm) and d - 3 mm (71 kV/cm). Values are given in Td. Shaded areas indicate approximate positions of the electrodes.

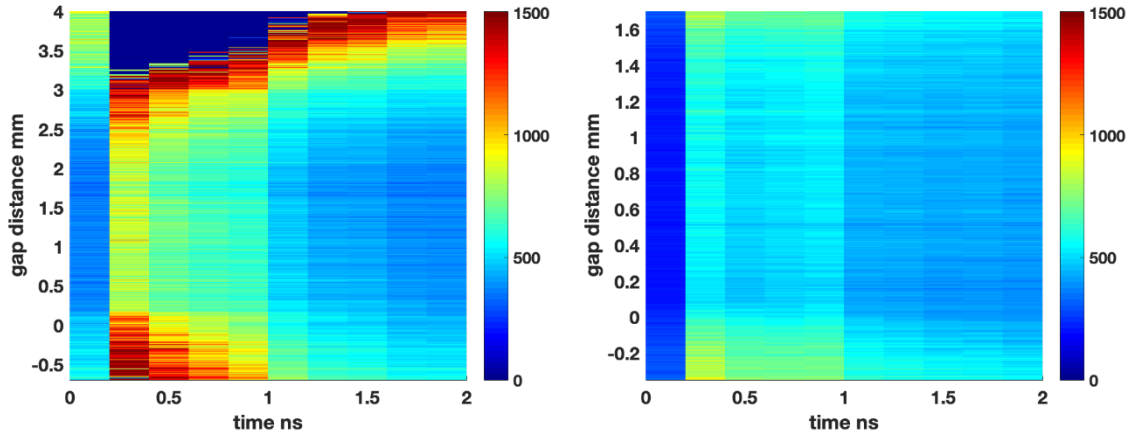

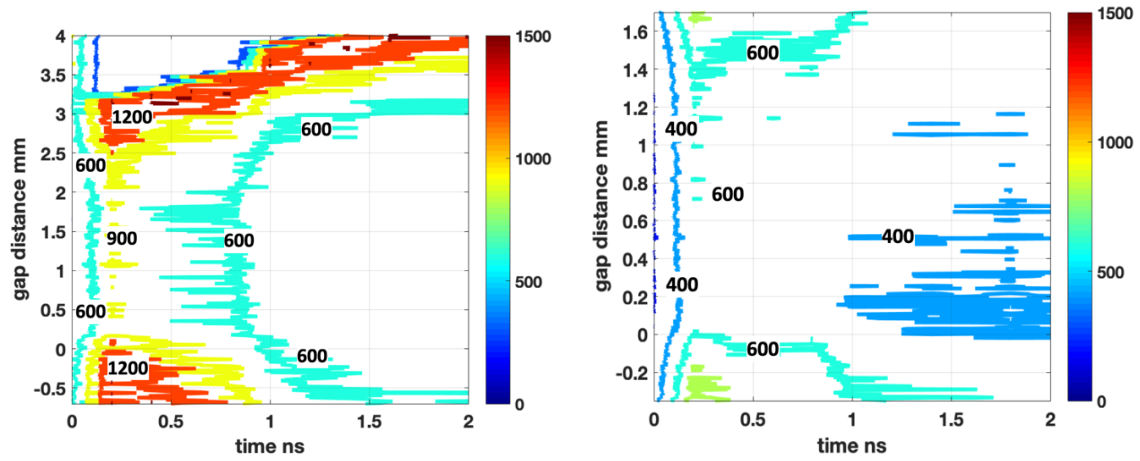

Figure 8. Enlarged reduced electric field strength distribution during the initial stage of the DBD: non-uniform mode (3 mm gap) on left compared to uniform (1.5 mm gap) mode on right.

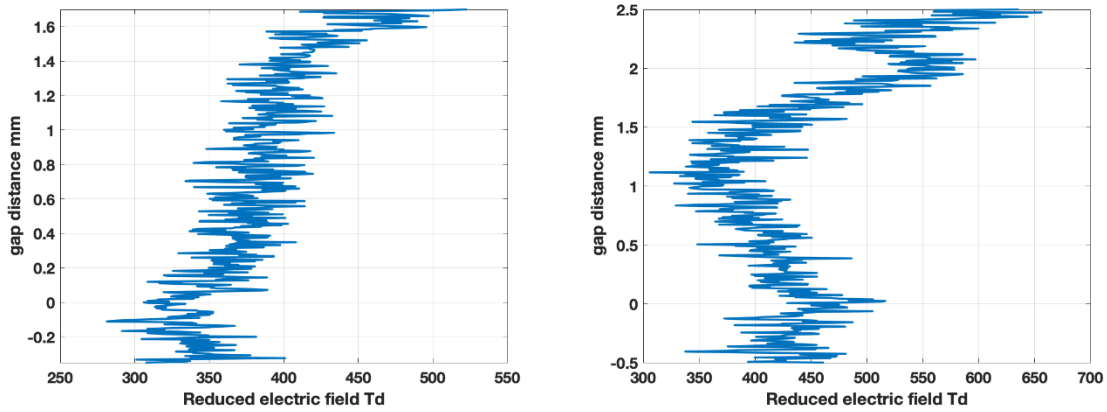

Figure 9. Distribution of the reduced electric field along the discharge gap from long-exposure measurements: 1.5 mm (left) and 2 mm (right) discharge gaps.

Conclusions

Here we report the experimental results on measurements of time and space resolved evolution of reduced electric filed in the atmospheric air dielectric barrier discharge ignited in two fundamentally different modes: non-uniform, ignited using relatively low applied electric fields, and uniform, which appears when condition of significant over-voltage is satisfied. Using passive approach of estimation of the reduced electric field strength values from the ratio of the emission intensities of the vibrational bands of nitrogen, we have demonstrated that conventional DBD, as expected, develops via cathode-directed streamers with corresponding maximum reduced electric field values of ~1200 Td (streamer head). In this case we clearly see the propagation of cathode-directed streamers in the discharge gap with the velocities of ~10^6 m/s. In contrast, in the case of significant overvoltage, the discharge emission appears uniform across the discharge gap and can qualitatively described as an absence of individual streamers with

corresponding lower maximum reduced electric field in the gap (~800 Td). This transition between the discharge modes was observed at applied electric field values of ~130 kV/cm and rise time of ~90 $kV \cdot cm^{-1} \cdot ns^{-1}$. We further hypothesize that this phenomenon of discharge ignition transition from Townsend to streamer to "overvoltage" modes, as the applied electric field value and its rise time increases, is not limited to the case of DBD, but is a fundamentally applicable to other discharge types. In our further studies we will attempt to check this suggestion, as well as understand the plasma chemistry of these modes which strongly depends on the discharge physics (and the local electric fields) and determines the applications of such plasmas.

Acknowledgment

The authors would like to thank Ronny Brandenburg and Tomáš Hoder for inspiring and useful discussions. This work was funded by the NSF/DOE Partnership in Basic Plasma Science and Engineering (DOE grant DE-SC0016492, PI: Dobrynin).

References

1. H Ayan et al 2008 IEEE Trans. Plasma Sci. vol 36 no 2 pp 504 -508
2. C Liu et al 2014 J. Phys. D: Appl. Phys. 47 252003
3. C Liu et al 2019 Plasma Res. Express 1 015007
4. U Kogelschatz 2003 Plasma Chem. Plasma Process 1 001
5. R Brandenburg 2017 Plasma Sources Sci. Technol. 26 053001
6. H-E Wagner et al 2003 Vacuum 71 03417
7. Low Temperature Plasma Technology: Methods and Applications, editors Paul K. Chu, XinPei Lu, CRC Press, Jul 15, 2013
8. S Kanasawa et al J. Phys. D: Appl. Phys. 1988 21 838.
9. T Nozaki et al 2002 Plasma Sources Sci. Technol. 11 431
10. R Tschiersch et al 2014 J. Phys. D: Appl. Phys. 47 365204
11. F Massines et al 2005 Plasma Phys. Control. Fusion 47 577
12. N Gheradi et al 2000 Plasma Sources Sci. Technol. 20 055015
13. Y Liu 2017 Physics of Plasmas 24 110701
14. B M Goldberg et al 2015 Plasma Sources Sci. Technol. **24** 035010
15. B M Goldberg et al 2016 Plasma Sources Sci. Technol. **25** 045008
16. M Simeni Simeni et al 2017 J. Phys. D: Appl. Phys. **50** 184002
17. Marc van der Schans et al 2017 Plasma Sources Sci. Technol. **26** 115006
18. P Böhm et al 2016 Plasma Sources Sci. Technol. **25** 054002
19. Benjamin M Goldberg et al 2015 Plasma Sources Sci. Technol. **24** 055017
20. Adam Obrusník et al 2018 Plasma Sources Sci. Technol. **27** 085013
21. Petr Bílek et al 2018 Plasma Sources Sci. Technol. **27** 085012
22. K V Kozlov et al 2001 J. Phys. D: Appl. Phys. 34 3164
23. T Hoder et al. 2016 Plasma Sources Sci. Technol. 25 045021
24. T Hoder et al. 2016 Plasma Sources Sci. Technol. 25 02517

25. T Hoder et al. 2015 Journal of Applied Physics 117 073302
26. G Dilecce et al 2007 Chem. Phys. Lett. 444 39
27. P Paris et al 2005 J. Phys. D: Appl. Phys. 38 3894
28. C O Laux 2002 Radiation and nonequilibrium collisional-radiative models Physico-Chemical Modeling of High Enthalpy and Plasma Flows (von Karman Institute Lecture Series 2002-07) ed D Fletcher et al (Belgium: Rhode-Saint-Genese)
29. S Goekce et al 2016 Plasma Sources Sci. Technol. 25 045002
30. S M Starikovskaia et al 2010 J. Phys. D: Appl. Phys. 43 124007
31. S A Stepanyan et al 2014 J. Phys. D: Appl. Phys. 47 485201
32. T Hoder et al 2017 Plasma Phys. Control. Fusion 59 074001